Multidomain simulations of aluminum nitride with machine-learned force fields

Drew Behrendt, Von Braun Nascimento,* and Andrew M. Rappe†
Department of Chemistry, University of Pennsylvania, Philadelphia, Pennsylvania 19104-6323, USA

(Received 6 September 2023; revised 13 June 2024; accepted 14 June 2024; published 19 July 2024)

Aluminum nitride (AlN) and other wurtzite materials are widely used in piezoelectric microelectromechanical systems and are of great interest for future thin-film ferroelectric devices. Much progress has been made by modeling these materials with quantum mechanical methods such as density functional theory (DFT). However, there are very few existing methods that can model AlN on a larger scale, and none that can model multiple phases and domain walls with the accuracy of DFT. In this work, we present a machine-learned molecular dynamics force field (MLFF) for AlN constructed by fitting an artificial neural network to an underlying DFT dataset. Using our trained MLFF, we can predict the energies, forces, and phonon dispersions of AlN with the accuracy of DFT at dramatically lower computational cost. Accordingly, our MLFF can simulate systems orders of magnitude larger than DFT, enabling the study of emergent and long-range effects, such as the frequency-dependent dielectric function and multiple ferroelectric domains. This method can easily be expanded to other wurtzite nitrides, oxides, and solid solutions.

DOI: 10.1103/PhysRevB.110.035204

I. INTRODUCTION

Aluminum nitride, along with dopants including scandium and boron, is used as the industry standard for radio frequency microelectromechanical systems that use film bulk acoustic resonators for mobile networks across the world due to Si compatibility, high piezoelectricity, and temperature stability [1–5]. Additionally, there is a growing interest in the potential for doped AlN to be used in thin-film ferroelectric devices for next-generation computing and other memory applications [6–12]. While these materials have long been studied using density functional theory (DFT) and other first-principles approaches, there is a great need to study emergent properties of this material class that require supercell sizes too large for DFT alone. While several classical molecular dynamics (MD) force fields have been proposed for AlN [13–17], there has yet to be developed a classical force field that can approach the accuracy of DFT and simultaneously study multiple phases and domain walls. While previous methods, predominantly fitted from experimental results for specific use cases, have shown great successes in their designed application, we aim to create a potential derived purely from *ab initio* data that can be used for many phases of AlN that have not been experimentally realized but may be essential for applications in ferroelectric domains.

In recent years, there has been an explosion in the use of machine learning (ML) to fit large datasets across many fields [18,19]. A particularly fruitful application of ML in materials science is in machine-learned force fields (MLFFs) for MD simulations, with simulations able to match DFT accuracy for up to 10 billion atoms [20]. Gaussian processes [21] and artificial neural networks (ANNs) [22–24] are developed to fit a large database of representative DFT snapshots of a material to a many-parameter classical potential based on local interactions of atoms with their neighbors. These methods have been used to model materials ranging from simple bulk insulators and metals to surfaces and layered materials [25–30]. In the present work, we choose an ANN approach to model AlN, due to the quick training and the relatively small increase in training time with increased dataset size and the number of element types [31]. Since we want to provide a potential that can readily be expanded to include many structures of interest, the ANN gives an advantage in quickly training over the large resultant datasets [31,32]. The aim of this work is to develop a reliable potential for AlN that can be used for future study of doped AlN, multidomain AlN, polarization switching, and other analogous wurtzite systems and properties.

II. METHODS

Because the trained MLFF will approach the accuracy of DFT, the details of the calculations included in the training set are very important to the overall model quality. DFT calculations were performed using Quantum Espresso [33] with optimized norm-conserving pseudopotentials from OPIUM [34,35]. The generalized gradient approximation (GGA) of Perdew, Burke, and Ernzerhof (PBE) was used to calculate the exchange-correlation energy [36]. All calculations were performed with an energy cutoff of 680 eV, with an energy convergence of 1.4×10^{-5} eV/cell, a force convergence cutoff of 2.6×10^{-4} eV/Å, and a $4 \times 4 \times 4$ k-point grid.

The DFT dataset was generated by taking snapshots of AlN in the wurtzite, zinc-blende, hexagonal boron nitride, cubic, and β-BeO phases, all with 32-atom unit cells (Fig. 1). For each non-wurtzite phase, 500 structures with random atomic displacements and strains were calculated with DFT. The random displacements were limited to 0.2 Å, and the strain was

*Also at Department of Physics, Federal University of Minas Gerais, Pampulha, Belo Horizonte, Minas Gerais 31270-901, Brazil.
†Contact author: rappe@sas.upenn.edu

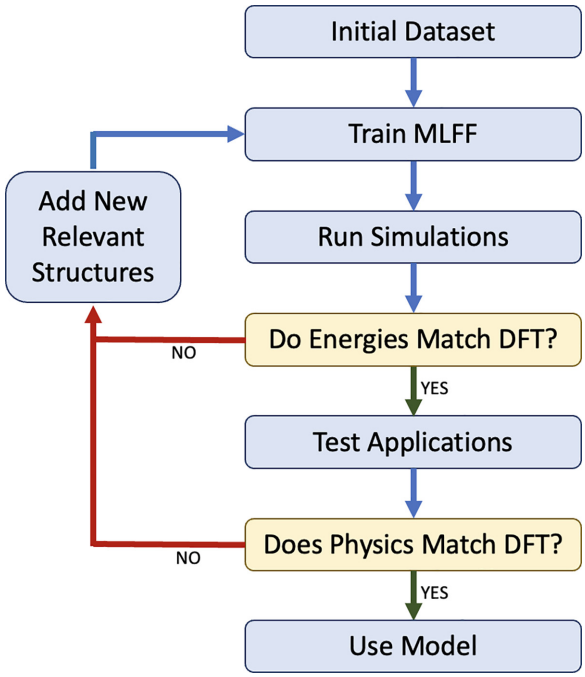

FIG. 1. Workflow for training a MLFF.

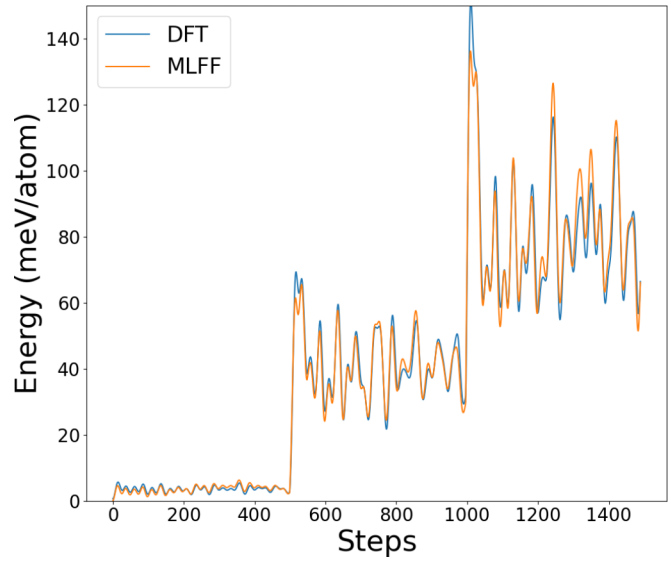

FIG. 2. Energy comparison between DFT and the trained MLFF over a MD trajectory at three different temperatures (50 K, 300 K, 600 K). Both the DFT and MLFF are shifted so that the lowest energy structure is at 0 meV/atom. The MD trajectories were not included in the training set for the MLFF.

limited to ±5%. Since we are primarily concerned with the wurtzite phase, 2000 random structures of wurtzite AlN were used. To capture the low-energy wurtzite configurations, *ab initio* molecular dynamics (ai-MD) using DFT was conducted for the wurtzite phase at 100 K, 300 K, and 600 K for 500 steps each. To improve the modeling of phonon modes, different supercells of the wurtzite phase with up to 108 atoms ($3 \times 3 \times 3$, $1 \times 1 \times 8$, $2 \times 1 \times 4$, etc.) were added and random displacements of those structures were included. Finally, we performed 7-step nudged elastic band (NEB) calculations of a switching pathway from N-polar to Al-polar AlN, and snapshots generated from the intermediate configurations were also added to the dataset. In total, just over 6400 snapshots of AlN were included in the final dataset. It is important to note that in the workflow described in Fig. 1, DFT snapshots were not generated in an automated fashion, and user intuition was required to select snapshots that represent the desired use-case of the potential. While this requires a certain level of expertise and knowledge of the desired uses, the described methodology can be extended to related systems (e.g., adding dopants) simply by adding more structures [31,37].

The ANN was trained using the AENET program [22], and classical molecular dynamics simulations were performed using AENET-LAMMPS [38,39]. The network was trained using four hidden layers, each containing 15 nodes with hyperbolic tangent activation functions. The ANN was trained with the Chebyshev basis set, with a cutoff of 8.0 Å for the radial expansion (expansion order of 12) and a cutoff of 6.5 Å for the angular expansion (expansion order of 6) [31]. The dataset was split, with 10% of the data used as a testing set and the rest was used for training with the L-BFGS-B algorithm [40]. The training continued until the root mean square errors (RMSEs) for both the training and testing sets are converged below 5 meV/atom.

The MLFF built off ANNs can also be easily expanded to include the effects of vacancies and dopants on the phase diagram and the material properties, as has been shown in previous applications [22,31,32].

III. PHYSICS TESTING

For the MLFF to provide physically meaningful MD simulations, we must assess its ability to model energies and forces for new structures of AlN to the same accuracy as DFT. Accordingly, we compared the energies between the MLFF and DFT for structures that were not in the training dataset. To do this, new ai-MD simulations were run at three different temperatures using the same DFT methods on an AlN supercell consisting of 16 atoms. The structures in these trajectories were then fed to the MLFF to compare the energies and the forces, with the energy comparison shown in Fig. 2. The energy difference between the MLFF and DFT has a RMSE of 3.5 meV/atom and never goes above 17 meV/atom, indicating that the MLFF reliably reproduces DFT energies for AlN configurations that were not included in the original training set.

In addition to the energy, the forces for each atom must match relatively well between the MLFF and DFT, to ensure that atomic movements generated with the MLFF will reproduce DFT MD closely. To investigate whether the forces are captured by the ANN, we used the 600 K ai-MD simulation and compared the forces for each atom in each Cartesian direction (Fig. 3). Even for this high-temperature simulation, the forces agree closely between the MLFF and DFT, indicating that the MLFF captures the shape of the potential energy surface for the active space of the wurtzite phase in AlN.

Beyond reproducing energies and forces from the training set, it is important that our MLFF can perform physically under various conditions, including strained states. To test

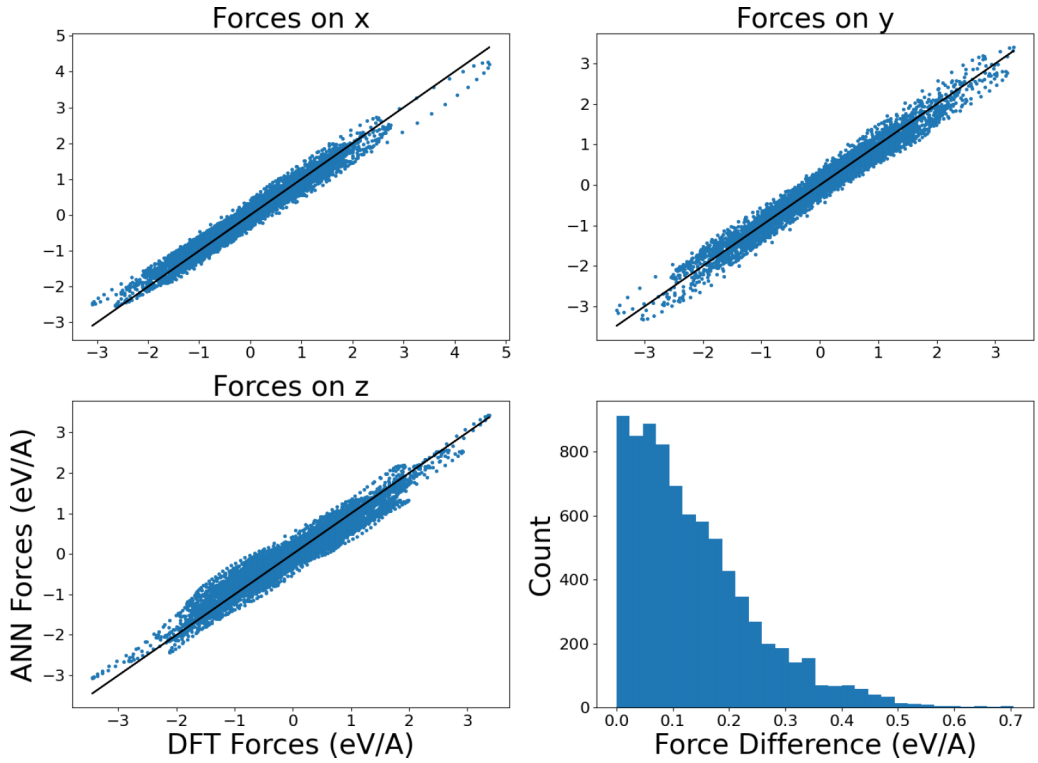

FIG. 3. Comparison of forces between MLFF and DFT based on structures generated during the ai-MD run at 600 K. Lower right panel shows a histogram of the distribution of the difference between forces calculated with MLFF and DFT. None of these structures were in the original training set for the MLFF.

whether our trained MLFF is comparable to DFT for new data and stable under *NPT* simulations, we generated an equation of state for five phases of AlN and compared the methods in Fig. 4. While uniaxial strain was primarily included in the training set, the volume in Fig. 4 was changed manually and the cell was allowed to relax cell parameters and atomic positions at the corresponding volume while maintaining the desired symmetry. The MLFF correctly predicts the energies for the strained states generated with DFT, and is stable under *NPT* simulations.

To explore the model properties further, we compare the phonon dispersion spectra of the wurtzite phase calculated using the MLFF and DFT models (Fig. 5). The spectra were calculated using finite displacements and a harmonic approximation with the ALAMODE program [41] and TO-LO splitting was included using the Parlinski approach [42]. While this second-order derivative information around local minima is not explicitly included in the training for the MLFF, it is still quite consistent with DFT, further validating that the MLFF captures the accuracy of DFT and the underlying physics of the wurtzite AlN. Phonon spectra comparisons for other secondary phases are included in the Supplemental Material [43] (see also Refs. [13–15,17,44,45] therein).

To test whether large unit cells simulated with the MLFF can accurately reproduce experimental observables for bulk AlN, we calculate the frequency-dependent dielectric function. To do this, we perform MD on a thermally equilibrated 4096 atom supercell under *NVE* conditions for 100 ps with 1 fs time steps. The macroscopic polarization is calculated using the atomic displacements from the layered hexagonal boron nitride phase multiplied by the born effective charge of the corresponding atom. Using this method, we calculate the spontaneous polarization to be 134 $\frac{\mu C}{cm^2}$ using both the

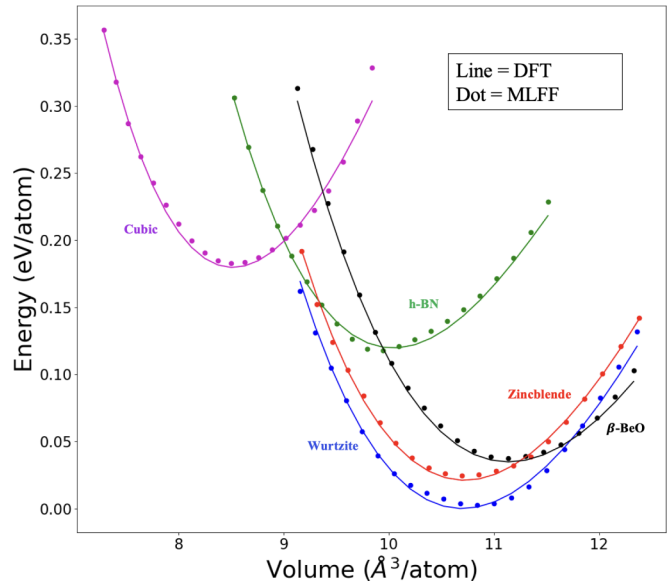

FIG. 4. Equations of state for the five major phases of bulk AlN using DFT and MLFF. For each volume and phase considered, we relax any internal coordinates not constrained by the phase space group, and we relax the relevant axis ratios, then both methods were used to calculate the energy of the optimized strained structures. None of the structures were in the original training set for the MLFF.

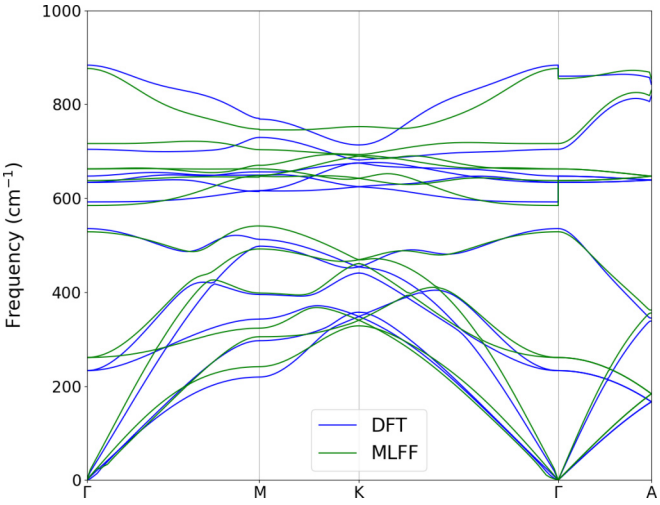

FIG. 5. Comparison of DFT and MLFF phonon dispersions calculated with finite atomic displacements [41]. A 72-atom unit cell was used.

MLFF and DFT, compared to 132 $\frac{\mu C}{cm^2}$ calculated with the Berry-phase method in DFT and approximately 150 $\frac{\mu C}{cm^2}$ from experiment [11]. For dielectric calculations, the polarization of the cell is collected every 10 fs, and the autocorrelation function of this time series is used to calculate the ionic part of the dielectric function using the Kubo-Green relation [46–48]. To calculate the full dielectric function, we added the optical part calculated with DFT, which is a constant over the considered frequency range. The wurtzite structure contains two unique axes, with $\epsilon_{xx} = \epsilon_{yy}$ and ϵ_{zz} being the only nonzero values in the dielectric tensor. The real part of the dielectric function is computed and plotted in Fig. 6. Note that the molecular dynamics does not capture TO-LO splitting. To

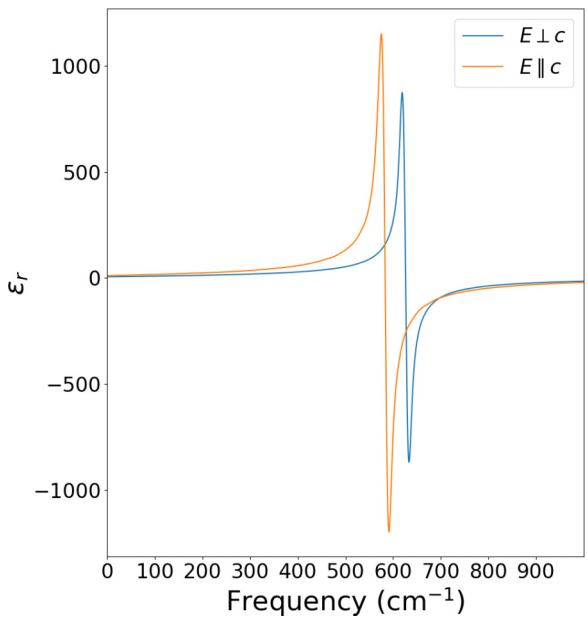

FIG. 6. Dielectric function for bulk aluminum nitride calculated from atomic trajectories generated with MLFF.

TABLE I. Comparison of phonon mode frequencies calculated using finite differences with both DFT and the MLFF, TO peaks fitted from MLFF dielectric function, and those deduced from IR and Raman transmission experiments [50,51].

Mode	IR Active?	Exp.	DFT	MLFF	ML-Dielectric
E_2 (low)	No	248	233	260	
B_1 (low)	No		535	529	
A_1 (TO)	Yes	610	592	584	575
E_2 (high)	No	655	634	638	
E_1 (TO)	Yes	667	647	662	641
B_1 (high)	No		704	716	
A_1 (LO)	Yes	888	860	855	
E_1 (LO)	Yes	910	883	876	

compare modes observed with our MLFF dielectric function to experiment and finite difference methods, we show the frequencies of the observed modes in Table I. The relatively low error and correct ordering of the axes further provide credence to the use of our potential to study macroscopic observables using the MLFF. In addition to the frequency-dependent dielectric response, we have calculated the optical dielectric response from our MLFF simulations. We find a zero frequency dielectric constant value of 10.9 which is in close agreement with experiments [49].

In order to test the temperature-dependent properties of the potential, we observe the melting temperature of our simulations and compare to experimental results. To do this, we perform an *NPT* simulation on a 8000-atom supercell with 1 bar of pressure and gradually increase the temperature. First the simulation was equilibrated to 1700 K, then the temperature in the Nosé-Hoover thermostat was increased to 1900 K over 1 000 000 time steps (1 ns). We deduce the simulation melting temperature to be the temperature at which the first Al-N bonds break and the ions start to flow freely, which in our simulation was 1725 K. Experimentally, AlN melts at 2100 K in vacuum and 2400 K under inert atmospheric pressure. Thus, our potential is stable even up to extremely high temperatures and realistically predicts both the lack of solid-solid phase transition and provides a rough estimation for the melting point.

IV. MULTIDOMAIN SIMULATIONS

Finally, we show that our force field is stable when simultaneously simulating multiple phases of AlN with domain walls. Previous studies have shown that the 180 degree domain wall between the Al- and N-polar phase interface of AlN is similar in structure to the β-BeO phase [12,52–54]. Additionally, this phase has been shown to be a possible intermediate in the switching pathway of B-doped AlN [55]. Therefore we added this structure to our training set in accordance with the training workflow (Fig. 1) in order to enable the simulations of AlN as a function of domain wall density and to probe the energy of different domain wall configurations. In Fig. 7, we show five possible domain wall densities initialized with our MLFF that are stable for over 100 ps at 300 K under *NVT* conditions.

While AlN has been used for decades as a piezoelectric, the novelty of ferroelectricity in doped AlN devices has thus far

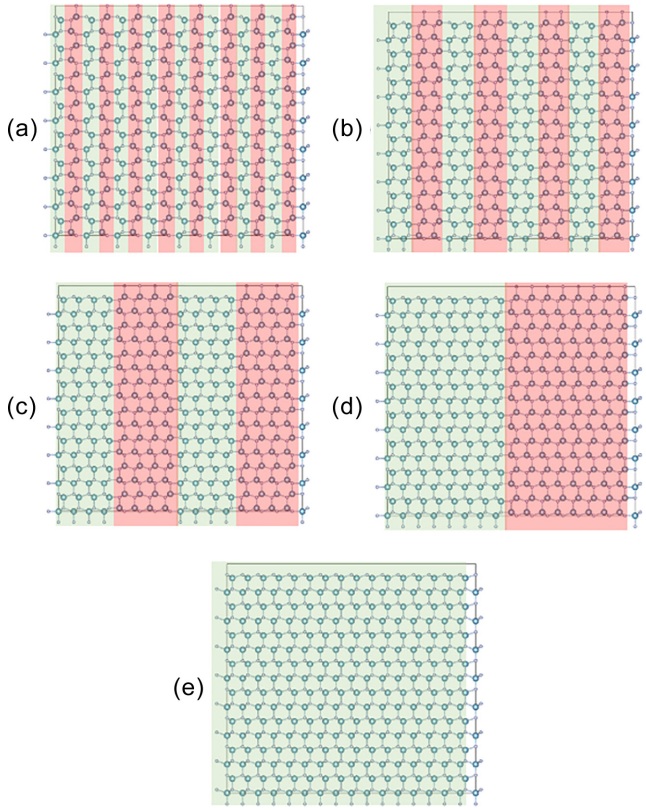

FIG. 7. Images of various domain wall densities and corresponding considered unit cells along the [100] direction. Green and red shaded areas represent up and down polarized regions of the material, respectively, for (a) 1.00, (b) 0.50, (c) 0.25, (d) 0.125, and (e) 0.00 domain walls per cell.

prevented in-depth analysis of domain wall energetics in AlN and other wurtzite materials. Here we show the first simulation of domain wall energy as a function of domain wall density in bulk AlN. To do this, we employ an $8 \times 8 \times 8$ AlN supercell of over 4000 atoms with our MLFF. The limit of high domain wall density in AlN is switching every other layer, which is equivalent to the β-BeO phase. The energies of these different domain wall densities in Fig. 7 per domain wall are listed in Table II. Clearly, the domain wall energy is not completely independent of the local domain environment. However, other than the wall stabilization shown by the β-BeO phase, the energy increase per wall is small and relatively constant when the density is changed. Additionally, the polarization reverses completely between adjacent domains no matter the density of the domain walls in the material. Thus, the domain walls

TABLE II. Energy for a domain wall for multiple domain wall densities. The domain wall density is defined as the number of domain walls per unit cell of AlN.

Wall Density	Wall Energy (mJ/m^2)
0.125	226
0.250	231
0.500	236
1.000	179

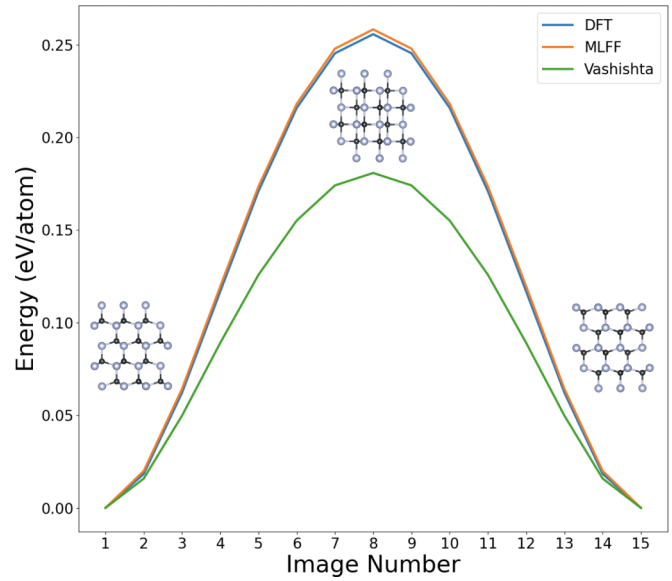

FIG. 8. NEB calculations for bulk switching pathway from polarization up to down calculated with DFT, the Vashishta potential, and our MLFF. Inset structures show the minimum and maximum energy structures along the pathway. Energy is relative to the minimum energy wurtzite structure.

in AlN are incredibly localized to the single unit cell limit. It is also important to note that due to the hexagonal symmetry, each line of atoms along the c axis can have 3 distinct domain walls and wall propagation can theoretically advance along any direction.

Thus, even though the domain wall energy in AlN is similar to traditional perovskites like lead titanate (208 mJ/m^2) [56], the domain walls in AlN are very different from other ferroelectrics. Only the 180 degree domain is possible due to symmetry and the polarization completely reverses over a single unit cell, which is not the same in perovskites [57], due to the stability and locality of the presence of the β-BeO phase at the boundary.

Additionally, to highlight the accuracy of the force field relative to existing potentials and DFT for the homogeneous switching pathway in addition to the heterogeneous pathway represented by the uncharged domain walls, here we show NEB calculations for DFT, MLFF, and the classical Vashishta potential (Fig. 8). The Vashishta potential is chosen to be representative of classical 3-body empirically fitted potentials. Because the MLFF can accurately match the energy of DFT for both models of switching and multidomain simulations, we are confident this model can accurately predict ferroelectric switching dynamics at the nm scale. Furthermore, the NEB switching barrier is much higher in energy than for even the densest domain wall configuration of the β-BeO phase (Figs. 4 and 8). The maximum slope of the NEB, using the atomic displacements between images, corresponds to the force to switch along this pathway, which can be converted to a maximum applied field for each method: 46.3, 46.2, and 31.4 MV/cm for DFT, MLFF, and Vashishta, respectively. While these pathways have been proposed previously as the switching mechanism from DFT [55], the extreme fields required to access these pathways show there must be lower

energy pathways that can only be accessed with simulations that require a classical potential with DFT-level accuracy. This adds further credence and importance of understanding domain wall density and interactions in the wurtzite structure and to the unique ability of this potential to explain more complicated and feasible switching mechanisms.

V. CONCLUSION

In summary, here we present an MLFF for bulk wurtzite and multiphase aluminum nitride. The MLFF correctly reproduces DFT energies and forces for structures that were not in the original dataset used for training, indicating that it can simulate bulk aluminum nitride at a fraction of the cost of DFT without sacrificing accuracy. For the 32-atom system, the MLFF is approximately 75 000 times faster than DFT. Additionally, the MLFF reproduced the phonon dispersion spectrum of AlN, even though the perturbed structures were not included in the training set. This potential was also able to produce the complex dielectric function with IR modes closely matching both DFT and experiment. The potential can be readily expanded to include dopants, vacancies, new phases, domain walls, and more; future work based on this MLFF has the potential to study emergent ferroelectric switching properties of this important material and provide insights that would not have been possible with DFT alone.

ACKNOWLEDGMENTS

D.B. acknowledges support of the U.S. Department of Energy, Office of Science, Office of Basic Energy Sciences, Energy Frontier Research Centers program, under Award No. DE-SC0021118, for study design, force field fitting, comparison with other force fields, and scientific insight. A.M.R. acknowledges the support of the Army Research Laboratory via the Collaborative for Hierarchical Agile and Responsive Materials (CHARM) under Cooperative Agreement No. W911NF-19-2-0119, for supervision and analysis of the proximity of polar and nonpolar phases. Computational support was provided by the High-Performance Computing Modernization Office of the Department of Defense and the National Energy Research Scientific Computing Center (NERSC), a U.S. Department of Energy Office of Science User Facility located at Lawrence Berkeley National Laboratory, operated under Contract No. DE-AC02-05CH11231. V.B.N. would like to acknowledge support from the FAPEMIG/MG Brazilian financial agency under Awards No. FAPEMIG RED-00458-16 and No. FAPEMIG APQ-01414-22, for analysis of machine-learning hyperparameters. V.B.N. would also like to acknowledge financial support from the Board of Trustees of the University of Pennsylvania. D.B. further acknowledges invaluable discussions about finite displacement phonon calculations with Atanu Samanta and dielectric function calculations with Jiahao Zhang.

[1] Y. Song, C. Perez, G. Esteves, J. S. Lundh, C. B. Saltonstall, T. E. Beechem, J. I. Yang, K. Ferri, J. E. Brown, Z. Tang, J. P. Maria, D. W. Snyder, R. H. Olsson, B. A. Griffin, S. E. Trolier-Mckinstry, B. M. Foley, and S. Choi, Thermal conductivity of aluminum scandium nitride for 5G mobile applications and beyond, ACS Appl. Mater. Interfaces **13**, 19031 (2021).

[2] M. Rubat du Merac, Transparent ceramics: Materials, processing, properties and applications, in *Encyclopedia of Materials: Technical Ceramics and Glasses*, edited by M. Pomeroy (Elsevier, Oxford, 2021), pp. 399–423.

[3] N. Li, C. P. Ho, S. Zhu, Y. H. Fu, Y. Zhu, and L. Y. T. Lee, Aluminium nitride integrated photonics: A review, Nanophotonics **10**, 2347 (2021).

[4] S. Strite and H. Morkoç, GaN, AlN, and InN: A review, J. Vac. Sci. Technol. B **10**, 1237 (1992).

[5] C. Fei, X. Liu, B. Zhu, D. Li, X. Yang, Y. Yang, and Q. Zhou, AlN piezoelectric thin films for energy harvesting and acoustic devices, Nano Energy **51**, 146 (2018).

[6] W. Zhu, J. Hayden, F. He, J. I. Yang, P. Tipsawat, M. D. Hossain, J. P. Maria, and S. Trolier-McKinstry, Strongly temperature dependent ferroelectric switching in AlN, $Al_{1-x}Sc_xN$, and $Al_{1-x}B_xN$ thin films, Appl. Phys. Lett. **119**, 062901 (2021).

[7] C. L. Cunha, T. C. Pimenta, and M. A. Fraga, Development and applications of aluminum nitride thin film technology, in *Thin Films*, edited by D. Yang (IntechOpen, Rijeka, 2022), Chap. 9.

[8] S. Yasuoka, T. Shimizu, A. Tateyama, M. Uehara, H. Yamada, M. Akiyama, Y. Hiranaga, Y. Cho, and H. Funakubo, Effects of deposition conditions on the ferroelectric properties of $(Al_{1-x}Sc_x)N$ thin films, J. Appl. Phys. **128**, 114103 (2020).

[9] S. Fichtner, N. Wolff, F. Lofink, L. Kienle, and B. Wagner, AlScN: A III-V semiconductor based ferroelectric, J. Appl. Phys. **125**, 114103 (2019).

[10] M. Noor-A-Alam, O. Z. Olszewski, and M. Nolan, Ferroelectricity and large piezoelectric response of AlN/ScN superlattice, ACS Appl. Mater. Interfaces **11**, 20482 (2019).

[11] J. Hayden, M. D. Hossain, Y. Xiong, K. Ferri, W. Zhu, M. V. Imperatore, N. Giebink, S. Trolier-McKinstry, I. Dabo, and J. P. Maria, Ferroelectricity in boron-substituted aluminum nitride thin films, Phys. Rev. Mater. **5**, 044412 (2021).

[12] Z. Liu, X. Wang, X. Ma, Y. Yang, and D. Wu, Doping effects on the ferroelectric properties of wurtzite nitrides, Appl. Phys. Lett. **122**, 122901 (2023).

[13] M. Tungare, Y. Shi, N. Tripathi, P. Suvarna, and F. Shahedipour-Sandvik, A Tersoff-based interatomic potential for wurtzite AlN, Phys. Status Solidi A **208**, 1569 (2011).

[14] P. Vashishta, R. K. Kalia, A. Nakano, and J. P. Rino, Interaction potential for aluminum nitride: A molecular dynamics study of mechanical and thermal properties of crystalline and amorphous aluminum nitride, J. Appl. Phys. **109**, 033514 (2011).

[15] K. Choudhary, T. Liang, K. Mathew, B. Revard, A. Chernatynskiy, S. R. Phillpot, R. G. Hennig, and S. B. Sinnott, Dynamical properties of AlN nanostructures and heterogeneous interfaces predicted using COMB potentials, Comput. Mater. Sci. **113**, 80 (2016).

[16] J. M. Sestito, M. Kempner, T. A. L. Harris, E. Zarkadoula, and Y. Wang, Development of aluminum scandium nitride molecular dynamics force fields with scalable multi-objective Bayesian optimization, JOM **74**, 3487 (2022).

[17] H. Xiang, H. Li, and X. Peng, Comparison of different interatomic potentials for MD simulations of AlN, Comput. Mater. Sci. **140**, 113 (2017).

[18] J. Wei, X. Chu, X. Y. Sun, K. Xu, H. X. Deng, J. Chen, Z. Wei, and M. Lei, Machine learning in materials science, InfoMat **1**, 338 (2019).

[19] G. Pilania, Machine learning in materials science: From explainable predictions to autonomous design, Comput. Mater. Sci. **193**, 110360 (2021).

[20] Z. Guo, D. Lu, Y. Yan, S. Hu, R. Liu, G. Tan, N. Sun, W. Jiang, L. Liu, Y. Chen, L. Zhang, M. Chen, H. Wang, and W. Jia, Extending the limit of molecular dynamics with *ab initio* accuracy to 10 billion atoms, in *PPoPP '22: Proceedings of the 27th ACM SIGPLAN Symposium on Principles and Practice of Parallel Programming* (Association for Computing Machinery, 2022), pp. 205–218.

[21] C. E. Rasmussen, Gaussian processes in machine learning, in *Advanced Lectures on Machine Learning: ML Summer Schools 2003, Canberra, Australia, February 2–14, 2003, Tübingen, Germany, August 4–16, 2003, Revised Lectures*, edited by O. Bousquet, U. von Luxburg, and G. Rätsch (Springer, Berlin, 2004), pp. 63–71.

[22] N. Artrith and A. Urban, An implementation of artificial neural-network potentials for atomistic materials simulations: Performance for TiO_2, Comput. Mater. Sci. **114**, 135 (2016).

[23] L. Zhang, J. Han, H. Wang, R. Car, and W. E, Deep potential molecular dynamics: A scalable model with the accuracy of quantum mechanics, Phys. Rev. Lett. **120**, 143001 (2018).

[24] J. Vandermause, S. B. Torrisi, S. Batzner, Y. Xie, L. Sun, A. M. Kolpak, and B. Kozinsky, On-the-fly active learning of interpretable Bayesian force fields for atomistic rare events, npj Comput. Mater. **6**, 20 (2020).

[25] J. Wu, L. Bai, J. Huang, L. Ma, J. Liu, and S. Liu, Accurate force field of two-dimensional ferroelectrics from deep learning, Phys. Rev. B **104**, 174107 (2021).

[26] L. Zhang, D.-Y. Lin, H. Wang, R. Car, and W. E, Active learning of uniformly accurate interatomic potentials for materials simulation, Phys. Rev. Mater. **3**, 023804 (2019).

[27] L. Zhang, M. Chen, X. Wu, H. Wang, W. E, and R. Car, Deep neural network for the dielectric response of insulators, Phys. Rev. B **102**, 041121(R) (2020).

[28] Y. Zhang, H. Wang, W. Chen, J. Zeng, L. Zhang, H. Wang, and W. E, DP-GEN: A concurrent learning platform for the generation of reliable deep learning based potential energy models, Comput. Phys. Commun. **253**, 107206 (2020).

[29] Q. Tong, P. Gao, H. Liu, Y. Xie, J. Lv, Y. Wang, and J. Zhao, Combining machine learning potential and structure prediction for accelerated materials design and discovery, J. Phys. Chem. Lett. **11**, 8710 (2020).

[30] Y. Shao, M. Hellstrom, P. D. Mitev, L. Knijff, and C. Zhang, PiNN: A Python library for building atomic neural networks of molecules and materials, J. Chem. Inf. Model. **60**, 1184 (2020).

[31] N. Artrith, A. Urban, and G. Ceder, Efficient and accurate machine-learning interpolation of atomic energies in compositions with many species, Phys. Rev. B **96**, 014112 (2017).

[32] O. T. Unke, S. Chmiela, H. E. Sauceda, M. Gastegger, I. Poltavsky, K. T. Schütt, A. Tkatchenko, and K.-R. Müller, Machine learning force fields, Chem. Rev. **121**, 10142 (2021).

[33] P. Giannozzi, S. Baroni, N. Bonini, M. Calandra, R. Car, C. Cavazzoni, D. Ceresoli, G. L. Chiarotti, M. Cococcioni, I. Dabo, A. D. Corso, S. de Gironcoli, S. Fabris, G. Fratesi, R. Gebauer, U. Gerstmann, C. Gougoussis, A. Kokalj, M. Lazzeri, L. Martin-Samos, N. Marzari, F. Mauri, R. Mazzarello, S. Paolini, A. Pasquarello, L. Paulatto, C. Sbraccia, S. Scandolo, G. Sclauzero, A. P. Seitsonen, A. Smogunov, P. Umari, and R. M. Wentzcovitch, QUANTUM ESPRESSO: A modular and open-source software project for quantum simulations of materials, J. Phys.: Condens. Matter **21**, 395502 (2009).

[34] A. M. Rappe, K. M. Rabe, E. Kaxiras, and J. D. Joannopoulos, Optimized pseudopotentials, Phys. Rev. B **41**, 1227 (1990).

[35] N. J. Ramer and A. M. Rappe, Designed nonlocal pseudopotentials for enhanced transferability, Phys. Rev. B **59**, 12471 (1999).

[36] J. P. Perdew, K. Burke, and M. Ernzerhof, Generalized gradient approximation made simple, Phys. Rev. Lett. **77**, 3865 (1996).

[37] A. M. Miksch, T. Morawietz, J. Kästner, A. Urban, and N. Artrith, Strategies for the construction of machine-learning potentials for accurate and efficient atomic-scale simulations, Mach. Learn.: Sci. Technol. **2**, 031001 (2021).

[38] M. S. Chen, T. Morawietz, H. Mori, T. E. Markland, and N. Artrith, AENET-LAMMPS and AENET-TINKER: Interfaces for accurate and efficient molecular dynamics simulations with machine learning potentials, J. Chem. Phys. **155**, 074801 (2021).

[39] A. P. Thompson, H. M. Aktulga, R. Berger, D. S. Bolintineanu, W. M. Brown, P. S. Crozier, P. J. in 't Veld, A. Kohlmeyer, S. G. Moore, T. D. Nguyen, R. Shan, M. J. Stevens, J. Tranchida, C. Trott, and S. J. Plimpton, LAMMPS—a flexible simulation tool for particle-based materials modeling at the atomic, meso, and continuum scales, Comput. Phys. Commun. **271**, 108171 (2022).

[40] R. H. Byrd, P. Lu, J. Nocedal, and C. Zhu, A limited memory algorithm for bound constrained optimization, SIAM J. Sci. Comput. **16**, 1190 (1995).

[41] T. Tadano, Y. Gohda, and S. Tsuneyuki, Anharmonic force constants extracted from first-principles molecular dynamics: Applications to heat transfer simulations, J. Phys.: Condens. Matter **26**, 225402 (2014).

[42] K. Parlinski, Z. Q. Li, and Y. Kawazoe, Parlinski, Li, and Kawazoe reply, Phys. Rev. Lett. **81**, 3298 (1998).

[43] See Supplemental Material at http://link.aps.org/supplemental/10.1103/PhysRevB.110.035204 for phonon dispersions of all major phases, discussion of polarization calculation methods, and comparison to other existing MD potentials.

[44] Y. Karaaslan, H. Yapicioglu, and C. Sevik, Assessment of thermal transport properties of group-III nitrides: A classical molecular dynamics study with transferable Tersoff-type interatomic potentials, Phys. Rev. Appl. **13**, 034027 (2020).

[45] F. Bernardini, V. Fiorentini, and D. Vanderbilt, Accurate calculation of polarization-related quantities in semiconductors, Phys. Rev. B **63**, 193201 (2001).

[46] R. Kubo, Statistical-mechanical theory of irreversible processes. I. General theory and simple applications to magnetic and conduction problems, J. Phys. Soc. Jpn. **12**, 570 (1957).

[47] M. P. Allen and D. J. Tildesley, *Computer Simulation of Liquids* (Oxford University Press, 2017).

[48] I. Ponomareva, L. Bellaiche, T. Ostapchuk, J. Hlinka, and J. Petzelt, Terahertz dielectric response of cubic $BaTio_3$, Phys. Rev. B **77**, 012102 (2008).

[49] J. S. Thorp, D. Evans, M. Al-Naief, and M. Akhtaruzzaman, The dielectric properties of aluminium nitride substrates for microelectronics packaging, J. Mater. Sci. **25**, 4965 (1990).

[50] J. G. Tischler and J. A Freitas, Anharmonic decay of phonons in strain-free wurtzite AlN, Appl. Phys. Lett. **85**, 1943 (2004).

[51] W. J. Moore, J. A. Freitas, R. T. Holm, O. Kovalenkov, and V. Dmitriev, Infrared dielectric function of wurtzite aluminum nitride, Appl. Phys. Lett. **86**, 141912 (2005).

[52] J. Casamento, S. M. Baksa, D. Behrendt, S. Calderon, D. Goodling, J. Hayden, F. He, L. Jacques, S. H. Lee, W. Smith, A. Suceava, Q. Tran, X. Zheng, R. Zu, T. Beechem, I. Dabo, E. C. Dickey, G. Esteves, V. Gopalan, M. D. Henry, J. F. Ihlefeld, T. N. Jackson, S. V. Kalinin, K. P. Kelley, Y. Liu, A. M. Rappe, J. Redwing, S. Trolier-McKinstry, and J.-P. Maria, Perspectives and progress on wurtzite ferroelectrics: Synthesis, characterization, theory, and device applications, Appl. Phys. Lett. **124**, 080501 (2024).

[53] T. S. Herng, A. Kumar, C. S. Ong, Y. P. Feng, Y. H. Lu, K. Y. Zeng, and J. Ding, Investigation of the non-volatile resistance change in noncentrosymmetric compounds, Sci. Rep. **2**, 587 (2012).

[54] L. Hromadová and R. Martoňák, Pressure-induced structural transitions in BN from *ab initio* metadynamics, Phys. Rev. B **84**, 224108 (2011).

[55] S. Calderon, J. Hayden, S. M. Baksa, W. Tzou, S. Trolier-McKinstry, I. Dabo, J.-P. Maria, and E. C. Dickey, Atomic-scale polarization switching in wurtzite ferroelectrics, Science **380**, 1034 (2023).

[56] S. Liu, I. Grinberg, H. Takenaka, and A. M. Rappe, Reinterpretation of the bond-valence model with bond-order formalism: An improved bond-valence-based interatomic potential for $PbTiO_3$, Phys. Rev. B **88**, 104102 (2013).

[57] Y.-H. Shin, I. Grinberg, I.-W. Chen, and A. M. Rappe, Nucleation and growth mechanism of ferroelectric domain-wall motion, Nature (London) **449**, 881 (2007).